

Optical bound states in the continuum enabled by magnetic resonances coupled to a mirror

Guoce Yang¹, Sukrith U. Dev², Monica S. Allen², Jeffery W. Allen², Hayk Harutyunyan^{1,}*

¹Department of Physics, Emory University, Atlanta, GA 30322, USA

²Air Force Research Laboratory, Munitions Directorate, Eglin AFB, FL 32542, USA

*Email:hayk.harutyunyan@emory.edu

ABSTRACT

Dielectric metasurfaces made of high refractive index and low optical loss materials have emerged as promising platforms to achieve high-quality factor modes enabling strong light-matter interaction. Bound states in the continuum have shown potential to demonstrate narrow spectral resonances, but often require asymmetric geometry and typically feature strong polarization dependence, complicating fabrication and limiting practical applications. We introduce a novel approach for designing high-quality bound states in the continuum using magnetic dipole resonances coupled to a mirror. The resulting metasurface has simple geometric parameters requiring no broken symmetry. To demonstrate the unique features of our photonic platform we show a record-breaking third harmonic generation efficiency from the metasurface benefiting from the strongly enhanced electric field at high-quality resonances. Our approach mitigates the shortcomings of previous platforms with simple geometry enabling facile and

large-area fabrication of metasurfaces paving the way for applications in optical sensing, detection, quantum photonics, and nonlinear devices.

KEYWORDS: high-Q resonance, BICs, metasurfaces, optical perfect absorber, nonlinear optics, third harmonic generation

TEXT

Optical resonators with high quality factors (Q factors) can trap optical modes, strongly enhance electric fields, and boost light-matter interaction. High-index dielectric resonant metasurfaces can achieve high-Q resonances due to the low optical loss, confined and enhanced electric field in dielectric resonators¹, and various mechanisms that minimize the radiative leakage including using high-order modes^{2,3}, Fano interference⁴⁻⁷, and bound states in the continuum (BICs)⁸⁻¹⁰. BICs, originally proposed in atomic systems¹¹, have recently been applied to guide the design of nanophotonic systems with novel functionalities¹²⁻¹⁵. BICs are localized wave states that exist in the continuous extended spectral region and do not exchange energy with free space. Thus, they have two unique defining features *viz.* infinitely long lifetime and infinitely high Q factor. Ideal BICs cannot be directly excited by far-field radiation, but “quasi BICs” were proposed to allow the leakage of small radiation into free space by tuning their geometry⁹ or excitation parameters¹⁶⁻¹⁹. Quasi BICs with finite but high Q factors have been used to construct resonant metasurfaces for applications including biosensors^{20,21}, lasers^{22,23}, and most recently, nonlinear optical processes²⁴⁻³⁰.

The main limitation of metasurfaces comprising quasi BIC modes working at normal incidence is the requirement of broken structural symmetry. Typically, this distorts the original symmetry-protected BIC modes and allows small radiative leakage which results in high-Q resonance⁹. Thus, accurately and reproducibly controlling the asymmetry is critical because both the Q factor and the resonant wavelength are very sensitive to the degree of asymmetry^{21,24}. This makes the nanofabrication of such platforms challenging. Furthermore, the symmetry breaking makes the high-Q resonances dependent on polarization angle of the incident light²⁵, which can be disadvantageous in applications that use nonpolarized light such as photodetection and imaging. In a symmetric nanodisk made of high-index materials, the in-plane magnetic dipole (MD) mode featuring a broadband resonance has been used for a perfect magnetic mirror³¹, phase control³² and the enhanced optical nonlinearity^{33,34}. In contrast, the out-of-plane magnetic dipole (MD) modes are natural quasi-nonradiative states but they can only be efficiently excited by azimuthally polarized light,³⁵⁻³⁷ which is not practical for most applications. Finally, most of the reported dielectric metasurfaces lack high-Q optical absorption, and are not suitable for applications such as hyper-/multi-spectral photodetection and thermal radiation control³⁸⁻⁴¹.

In this work, we have developed a simple approach for creating BIC modes using arrayed Si pillars to support radiative in-plane MD resonances on a reflecting mirror separated by a dielectric spacer layer. The evolution from ideal BICs to quasi BICs is controlled by metasurface-mirror distance and the size of Si pillars. These geometrical parameters are easily controlled using conventional fabrication methods without need of the broken geometric symmetry. A high-Q optical absorber governed by the BIC is theoretically proposed and experimentally realized in the metasurface. To further demonstrate the unique optical properties of the novel metasurface we study its performance as an efficient nonlinear platform to enhance

frequency conversion using third harmonic generation (THG). A large THG enhancement factor of up to 5×10^7 is observed compared to an unpatterned Si film. The conversion efficiency is 1.8×10^{-6} at a relatively low peak pump intensity of 0.4 GW/cm^2 .

A three-dimensional (3D) schematic of the designed metasurface is shown in Fig. 1a. The structure consists of Si pillar array on a gold ground film separated by a SiO_2 spacer layer. The Si pillars support various Mie resonances including a first-order in-plane MD resonance. This MD resonance of the metasurface is retrieved numerically (Eigenfrequency solver in COMSOL Multiphysics) and its electric and magnetic field distributions are shown in Fig. 1b. The circular loop shaped electric field and the horizontal in-plane dipole-like magnetic field are the critical characteristics of the MD resonant mode. The electric field of the mode is predominantly confined in the Si pillar, therefore the relatively large third-order nonlinear susceptibility of Si ($\chi^{(3)} = 2.8 \times 10^{-18} \text{ m}^2/\text{V}^2$) can be effectively utilized in nonlinear optical processes.

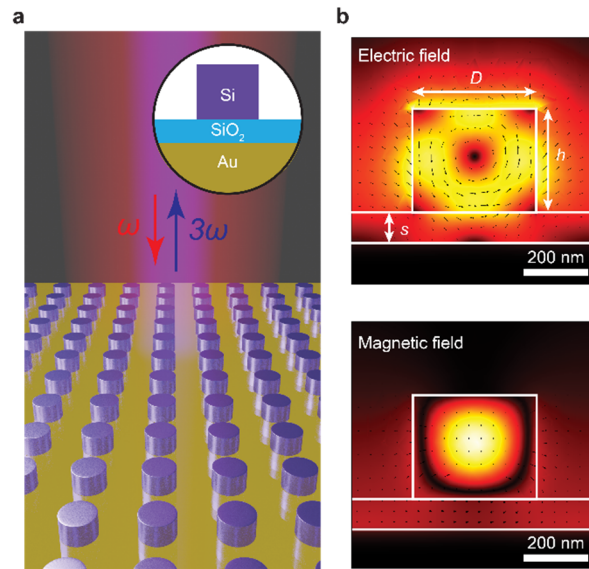


Figure 1. Si metasurface on a gold mirror. (a) 3D schematic of the metasurface. The inset shows the cross section of the unit element with corresponding materials. (b) Simulated electric field

and magnetic field distributions of the horizontal MD mode. The geometric parameters used in the simulation are the diameter of the pillars $D=340$ nm, height of the pillars $h=305$ nm, spacing $s=95$ nm, and the periods along both directions $2D=680$ nm.

The BIC in our proposed metasurface originates from the coupling between the MD resonator and its image due to the presence of a mirror, as shown in the inset of Fig. 2a. First, we use temporal coupled mode theory (TCMT) to demonstrate our approach by treating the ideal case analytically^{8,42}. Assuming that the mirror is a lossless perfect electric conductor (PEC), we can simplify our structure to a system with two identical horizontal magnetic dipole resonators separated by $2d$, where d is the distance between the center of Si pillar and the PEC mirror. The time evolution of the two resonators with amplitudes of a_1 and a_2 can be expressed by Eq. (1).

$$i \frac{\partial}{\partial t} \begin{bmatrix} a_1 \\ a_2 \end{bmatrix} = \left[\begin{bmatrix} \omega_0 & \kappa \\ \kappa & \omega_0 \end{bmatrix} - i \frac{\gamma_r}{2} \begin{bmatrix} 1 & -e^{i2kd} \\ -e^{-i2kd} & 1 \end{bmatrix} \right] \begin{bmatrix} a_1 \\ a_2 \end{bmatrix} \quad (1)$$

where ω_0 is the resonant frequency of each resonator, $\gamma_r/2$ is the radiative decay rate to the half space, k is the propagation constant between the resonators, and κ is the near-field coupling rate. The determined eigenvalues from Eq. (1) are $\omega_{\pm} = \omega_0 \pm \kappa + i\gamma_r[\pm \exp(i2kd) - 1]$ and the corresponding eigenvectors are $\psi_{\pm} = [1, \pm 1]^T$, respectively. It should be noted that the MD resonator and its image underneath the PEC mirror must be in phase. Therefore, the only meaningful eigenvector is $\psi_{+} = [1, 1]^T$ with the eigenfrequency of $\omega_{+} = \omega_0 + \kappa + i\gamma_r[\exp(i2kd) - 1]$. When the phase shift $2kd$ equals to 2π (or any integral multiple of 2π), the imaginary part of the eigenfrequency reaches zero and the eigenmode becomes a BIC which has an infinitely large quality factor. When the phase shift starts to detune from 2π , the eigenmode becomes a quasi-BIC mode with a non-zero imaginary part of the eigenfrequency and a large but finite quality factor.

Next, the eigenfrequency solver is used to calculate the complex eigenfrequencies of the MD mode in the metasurfaces with a PEC mirror. The results are plotted as dashed lines in Fig. 2a and 2b and the Q factor is defined by $Q = \text{Re}(\omega_+)/2\text{Im}(\omega_+)$. The imaginary part of the eigenfrequency reaches to almost zero and the corresponding Q factor reaches $\sim 10^7$ when the SiO₂ thickness is 105 nm. The maximum Q factor value is limited in the calculation by mesh size and tends to infinity for infinitely small mesh size resulting in an ideal BIC formation in the absence of radiative decay. Practical metals are not ideal PECs and introduce non-radiative loss in the system which deteriorates the Q factors. When the simulations are repeated by substituting PEC with a gold film, the properties of the system change as shown in Fig. 2a and 2b (solid lines). The resultant eigenfrequencies and Q factors have the same trend as the case with PEC except a minor shift due to the non-radiative loss. Eigenfrequency change induced by a lossy mirror is analyzed in Supporting Information, Note B. The imaginary part of the eigenfrequency has a non-zero minimum when SiO₂ thickness is 95 nm corresponding to the non-radiative loss in the metasurface system with a maximum Q factor reaching 800. Despite the non-zero imaginary part, the radiative decay disappears, indicating that the resonator does not exchange energy with free space similar to the lossless BIC mode. When detuning the thickness from this point the radiative decay starts to contribute to the imaginary part of the eigenfrequency and the Q factor decreases. Besides the SiO₂ thickness, the diameter of Si pillars can affect the phase shift $2kd$ because $k = n\omega_0/c$, where ω_0 is mainly determined by the diameter of Si pillars, n is the effective refractive index between the mirror and the center of the pillar, and c is the speed of light in the vacuum. Simulated results with varied Si pillar diameters are shown in Fig. 2c and 2d demonstrating that the BIC mode can be obtained by controlling diameters while keeping the SiO₂ spacer thickness fixed.

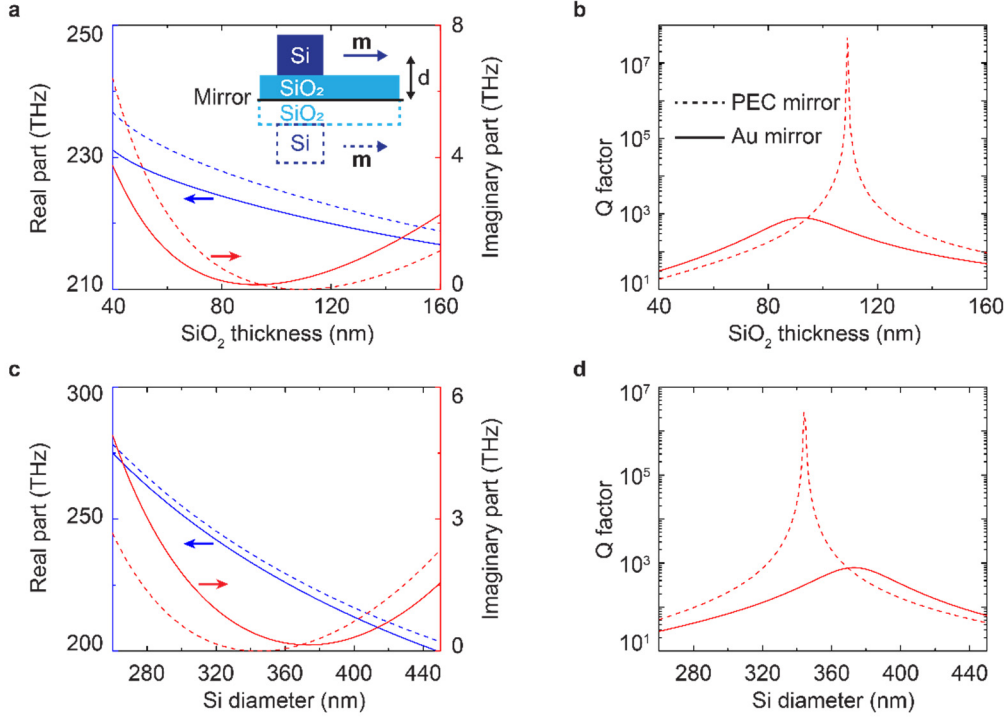


Figure 2. Theory of the BIC. (a) SiO₂ spacer thickness-dependent eigenfrequencies. In the simulations the diameter of Si pillars is 370 nm and the period is 740 nm. The inset shows the coupling between the MD resonance and its image. (b) Q factors as a function of SiO₂ spacer thickness. (c) Eigenfrequencies and (d) Q factors as a function of the Si pillars' diameter. In the simulations SiO₂ thickness is 95 nm and the period is 2 times of the diameter of Si pillars. In (a-d), dashed lines and solid lines represent two cases of using PEC mirror and gold mirror, respectively.

The reflectance of the metasurface can be approximated by a model,⁴² where the transmittance is ignored because of the 100 nm thick gold film. The reflectance is described by Eq. (2)

$$R = \frac{(\omega - \Omega)^2 + (\Gamma_r - \Gamma_{mr})^2}{(\omega - \Omega)^2 + (\Gamma_r + \Gamma_{mr})^2} \quad (2)$$

where $\Omega = \text{Re}(\omega_+)$ is the central resonant frequency of the whole metasurface system, Γ_r and Γ_{nr} denotes the radiative and the non-radiative rate of the system, and $\Gamma_r + \Gamma_{nr} = \text{Im}(\omega_+)$. The reflectance reaches minimum on resonance corresponding to the maximum of absorption (100%- R). The maximized absorption reaches 100% when $\Gamma_r = \Gamma_{nr}$, namely at the critical coupling condition, and we obtain a perfect absorber (PA) featuring high-Q resonance because of the existence of the BIC. Full-wave simulations are used to calculate the reflectance spectra of metasurfaces with different diameters of Si pillars and the same SiO₂ thickness (see Fig. 3a). At the special BIC point where the diameter is 370 nm (see Fig. 2c), there is no radiative leakage ($\Gamma_r = 0$) and, thus, the reflectance spectrum remains at 100%. However, the radiative rate Γ_r deviates from zero when the mode is detuned from the BIC point by changing the diameter. Two points PA1 and PA2 with the absorption of 100% are observed at the diameters of respectively 340 nm and 400 nm, where the critical coupling condition $\Gamma_r = \Gamma_{nr}$ is satisfied. The radiative rate Γ_r can also be controlled by the SiO₂ thickness, and simulated reflectance spectra with varied thicknesses and fixed diameter are shown in Supporting Information (Fig. S3) featuring a similar “PA1-BIC-PA2” transition.

The metasurface is fabricated using standard film deposition, electron beam lithography (EBL) and reactive ion etching (RIE) process (see Note A in Supporting Information for details). All metasurfaces have the same array size of $100 \times 100 \mu\text{m}^2$. The scanning electron microscopy (SEM) image of a representative Si array is shown in the inset of Fig. 3b. Without loss of generality, in this work we consider samples with varying Si pillar diameter (and not varying spacer thickness) to simplify fabrication. Fig. 3b shows the experimental reflectance spectra of the fabricated samples which are in a good agreement with the simulation results (Fig. 3a) and are exhibiting the same “PA1-BIC-PA2” transition. The only minor difference between

simulations and measurements is an extra middle resonant branch in the left-top region of the measured map. This additional resonant mode observed in the experiments results from the out-of-plane electric dipole mode excited by the oblique incident TM polarized light which provides the out-of-plane electric field component (see Supporting Information Fig. S4 for the analysis of reflectance spectra at different incidence angles). Even with an iris added at the back focal plane of the objective to reduce the numerical aperture, the oblique incident light with small incidence angles ($<2.5^\circ$) still contributes to the excitation out-of-plane modes in the experimental results. Three representative measured spectra corresponding to PA1, BIC and PA2 are plotted in Fig. 3c. There is no resonant dip observed in the reflectance spectrum of the metasurface with the diameter of 370 nm. The deepest resonant dips with the reflectance of 20% and 10% are found in the metasurface at the diameters of 340 nm and 400 nm and the full-width half-maximums (FWHMs) of the resonance are 7.5 nm and 5 nm corresponding to Q factors of 172 and 282, respectively, which are larger than those observed for various plasmonic narrowband PAs⁴³⁻⁴⁵. All extracted Q factors from the measured and simulated spectra with different pillar diameters are shown in Fig. 3d. The Q factor dependence as a function of the diameter follows the same trend as shown in the eigenfrequency analysis in Fig. 2d which further confirms the origin of the high-Q resonance as BICs induced by the MD mode. Experimentally extracted Q factors vary from 35 to ~ 600 depending on the pillar diameter, which is slightly lower than simulation values. This difference can be attributed to the fabrication imperfections and the limited array size. The fabrication imperfections include inhomogeneous diameters, which results in inhomogeneous broadening of the spectra, and the surface roughness and oxidation of Si pillars after dry and wet etching processes, which introduce optical loss at the surface. The roughness average (Ra) of Au film, SiO₂ film and Si film is 0.83 nm, 0.94 nm and 1.16 nm, respectively. The ultrasmooth

template stripping metal and van der Waals materials with the atomically smooth surface could be potential ways to further reduce the surface loss^{46,47}. On the other hand, the limited array size spatially cuts the periodical extension of the structure and, thus, allows more radiative channels, which further limits the Q factor. These factors can also result in the reduction of measured peak absorption compared with the simulations.

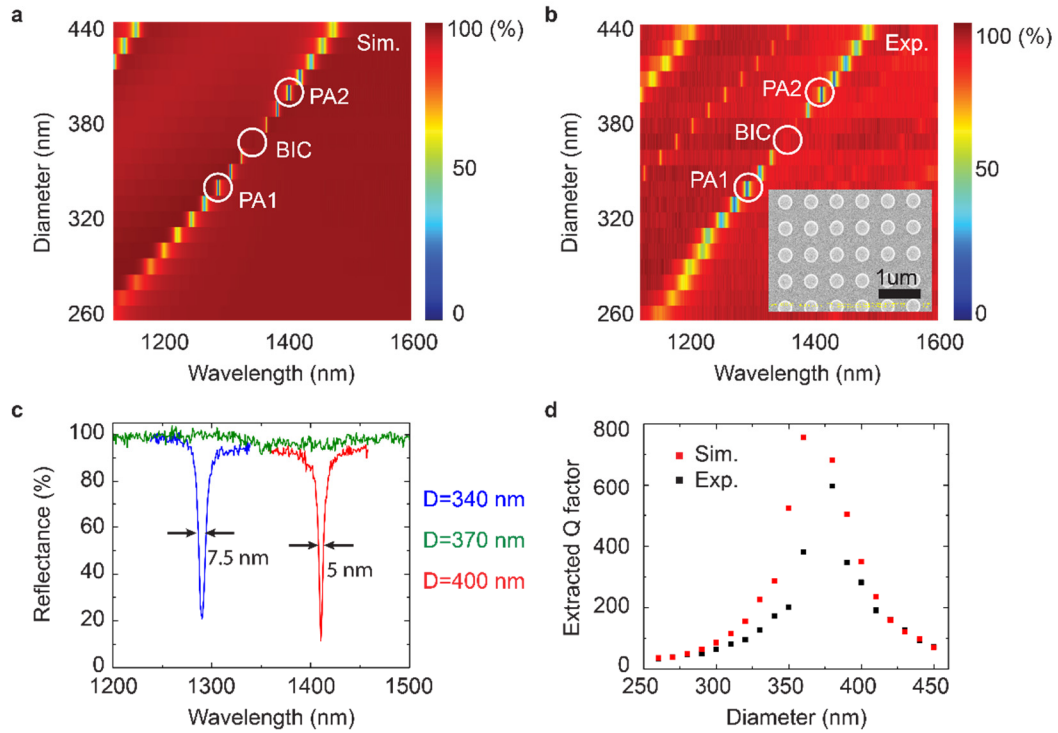


Figure 3. Linear reflectance spectra of the BIC metasurface. (a) Simulated reflectance spectra of the metasurface. SiO₂ thickness is 95 nm and the period is 2 times the diameter of Si pillars to keep the same fill fraction defined by the ratio of Si and total area. (b) Experimentally measured reflectance spectra of the metasurface. The inset shows the SEM image of the sample. (c) Three measured representative reflectance spectra corresponding to two PA cases (blue and red lines) and the BIC case (green line). (d) Extracted Q factors from simulated and experimentally measured reflectance spectra.

One of important applications benefiting from such a high-Q resonance is nonlinear frequency conversion as the harmonic generation is proportional to the local field enhancement. Here we demonstrate strongly enhanced THG from the BIC metasurface excited using femtosecond (fs) laser pulses. Fig. 4a and 4b show the pump wavelength-dependent THG from two metasurfaces with different pillar diameters of 340 nm and 300 nm featuring experimental Q factors of 172 and 64, respectively. A significant enhancement of THG at the metasurface resonance is observed. In both samples the THG intensity is maximized when the pump wavelength matches with the linear resonance of the metasurface and is dramatically decreases when the pump wavelength is off-resonance. Interestingly, the THG emission wavelength is more insensitive to the change of the pump wavelength for high-Q sample than it is for the low-Q metasurface (white dotted lines in Fig. 4a and 4b). Thus, the peak wavelength of the broadband fs THG emission does not always exactly equal to $1/3$ of the fundamental wavelength especially within the high-Q resonance region. This unusual feature is also demonstrated by full-wave nonlinear simulation of THG using finite-difference time-domain (FDTD) method (Fig. 4c and 4d). This can be attributed to the spectrally selective enhancement of the pump electric field by the resonance. For a high-Q resonance, the resonant bandwidth is comparable to and narrower than the spectral linewidth of the fs pump pulse. Thus, the wavelength corresponding to the maximum pump electric field is determined not only by the wavelength of the pump pulse in free space but also by the resonant wavelength of the metasurface. The effect is amplified with the increase of the Q factor.

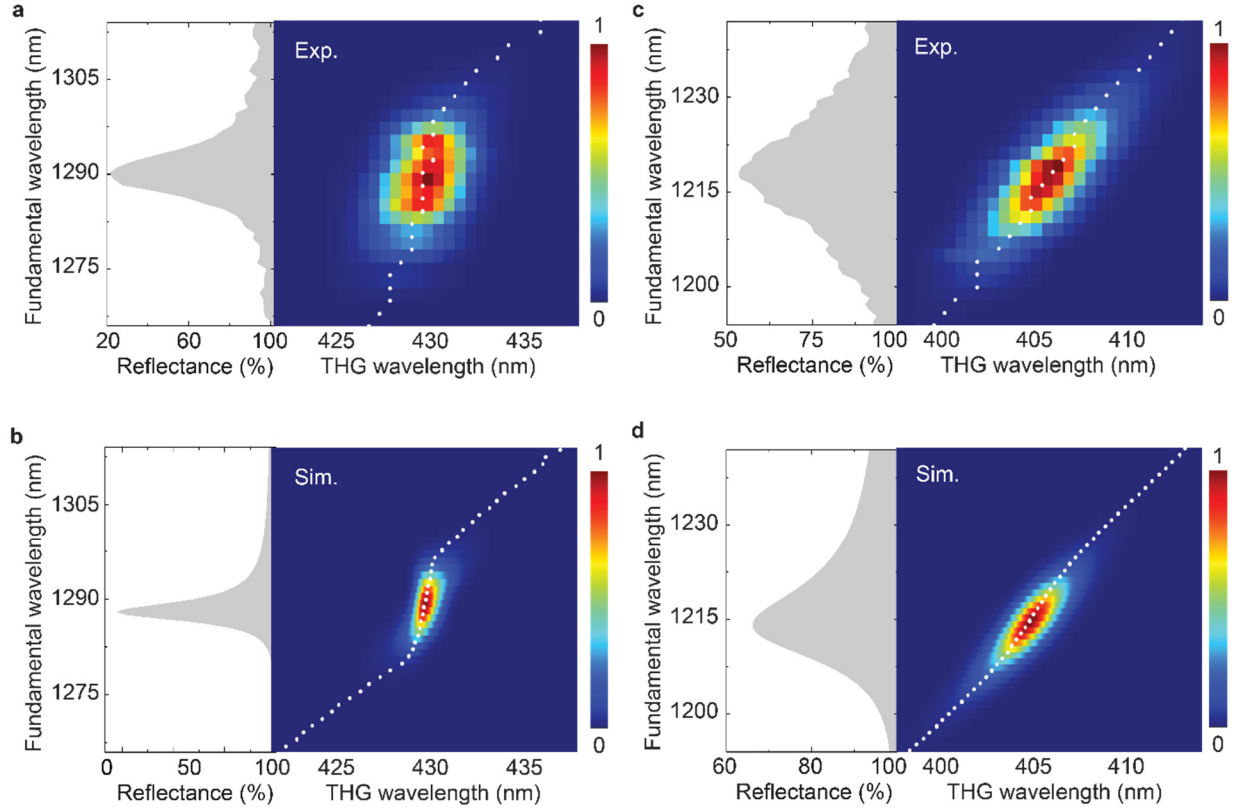


Figure 4. Fundamental wavelength-dependent THG spectra. The grey shaded areas show the linear reflection spectrum from the metasurface. The contour maps show the experimentally measured THG spectra from the sample at varied pump wavelengths. (a), (b) experimental results for Si pillar diameter of 340 nm and 300 nm, respectively, (c), (d) simulated results for the same geometry as in (a) and (b), respectively.

Next, we investigate the dependence of the maximum intensity THG wavelength on the pillar diameters. The measured and simulated results are shown in Fig. 5a. The maximum THG intensity has a similar trend compared with the peak absorption. In other words, the THG is maximized near the two PA points (Fig. 3a and b) corresponding to the critical coupling condition. This trend can be explained using TCMT as follows^{24,42}. At steady state and in the

nondepleted regime, assuming single frequency input, the THG power $P_{3\omega}$ is determined by Eq.

(3)

$$P_{3\omega} \propto |A_{\omega}|^6 = \left(\frac{2\Gamma_r}{(\omega - \Omega)^2 + (\Gamma_r + \Gamma_{nr})^2} \right)^6 P_{\omega}^3 \quad (3)$$

where A_{ω} denotes the amplitude of the resonant mode with the incident power P_{ω} at the frequency of ω . Therefore, the THG yield $P_{3\omega}/P_{\omega}^3$ on resonance reaches the maximum at the critical coupling point where $\Gamma_r = \Gamma_{nr}$, corresponding to the PA point of the metasurface. However, there is a small discrepancy between the linear and nonlinear results as both measured and simulated THG reach their local maxima for metasurfaces at the diameters of 320 nm and 440 nm, instead of 340 nm and 400 nm where critical coupling occurs. This can be attributed to the broader linewidth of the pump laser. With the increased duration time of the input pulse in simulations, resultant THG has the local maximum at the diameter of 340 nm and 400 nm (see Supporting Information, Fig. S5). The difference of THG intensity between the two critical coupling regions can be attributed to the slightly different electric field enhancement (see Supporting Information, Fig. S6).

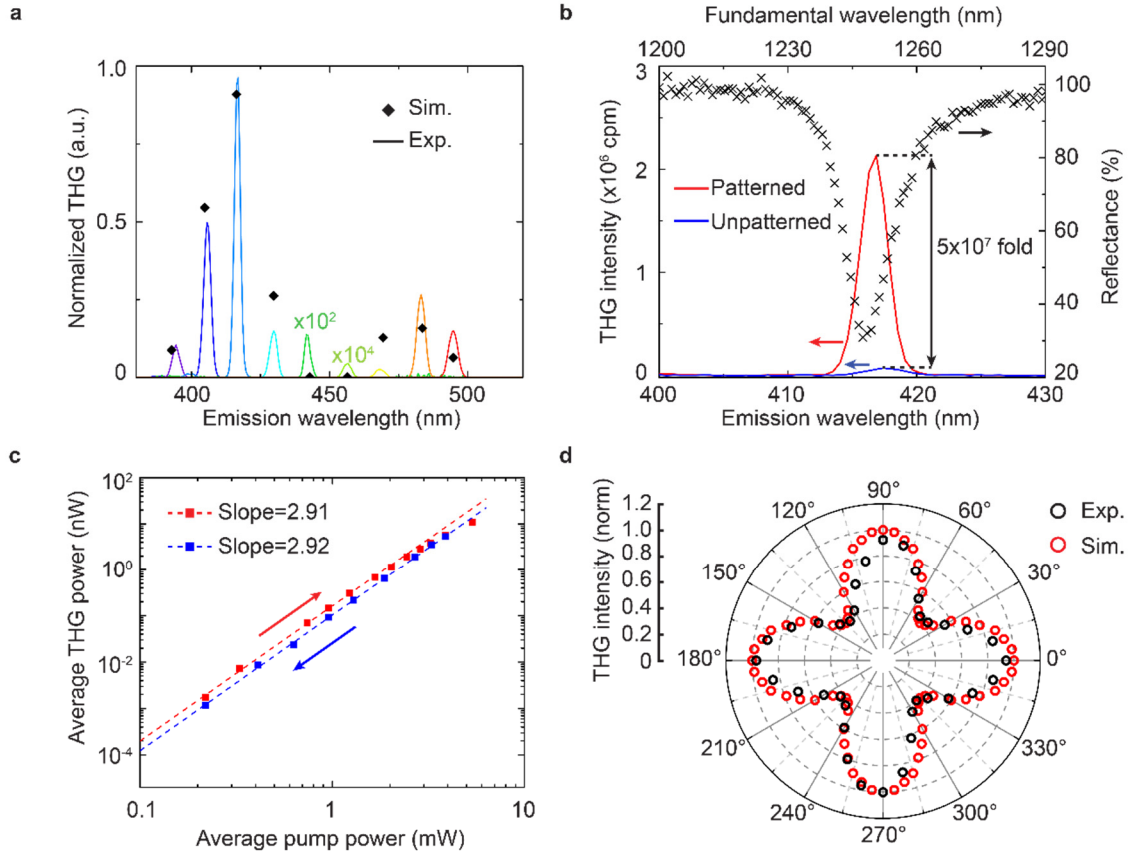


Figure 5. Efficient THG conversion. (a) Simulated and experimentally measured THG intensities from metasurfaces with different Si pillar diameters. The curves represent measured spectra for diameters from 280 nm to 440 nm (20 nm step). (b) Measured THG spectra from the patterned metasurface ($D=320$ nm) and the unpatterned Si film on the same sample. The blue spectrum has been multiplied by 100 for clarity. The pump power is 0.55 mW on the metasurface and 13 mW on the Si film. (c) Log-log plot of measured average THG power from the same sample in (b) as a function of average pump power. Red and blue markers are measured points upon increasing and decreasing the pump power, respectively. Dashed lines represent the linear fitting results in the log-log plot and the slopes close to 3 reflect the cubic power dependence. (d) Simulated and experimentally measured THG intensities from the same sample as in (b) pumped by light beam with different linear polarization angles. The nonlinear results in (b-d) are all

acquired at the fundamental wavelength of 1250 nm corresponding to the linear resonance of the metasurface.

To estimate the nonlinear signal enhancement we choose a metasurface ($D=320$ nm) with the highest observed THG. Compared to the unpatterned Si film on the same sample, the metasurface has a strong THG with an enhancement factor of 5×10^7 shown in Fig. 5b.

Furthermore, the THG power as a function of the pump power is plotted in Fig. 5c. With the increased pump power, the THG power increases following the cubic law and starts to saturate at the average pump power of 5.3 mW corresponding to the peak power of 331 W (considering the pulse length of 200 fs and the repetition rate of 80 MHz) and the peak power density of 0.4 GW/cm² (considering the laser spot diameter of 10 μ m). When reversing the measurement to decrease the pump power, we find a similar cubic law dependence with a reduced THG intensities. This reduced THG output can point to the starting damage of the sample (see Supporting Information, Fig. S8), possibly due to the melting of the gold film induced by the strong absorption in the metal. The total absolute conversion efficiency defined by $P_{3\omega, \text{peak}}/P_{\omega, \text{peak}}$ can be estimated to be 1.8×10^{-6} at the average pump power of 5.3 mW, where the subscript “peak” denotes the peak power. The normalized conversion efficiency defined by $P_{3\omega, \text{peak}}/P_{\omega, \text{peak}}^3$ is $1.6 \times 10^{-11}/\text{W}^2$. To the best of our knowledge, both efficiencies are the highest reported values using fs pulsed laser. The calibration method of the measured THG power is described in Supporting Information, Note G. Finally, polarization dependence of the THG signal is shown in Fig. 5d. The experimental results are in a good agreement with the simulations. In contrast to previously reported BIC and Fano metasurfaces with broken symmetries, our proposed structures have geometric symmetry and therefore there is no significant THG difference between two orthogonal pump polarizations. The THG intensity diminishes for polarization angles not aligned

with the periodicity of the array reaching a minimum for 45° angle due to the C4 symmetry of the array. The minimum THG is still as high as 40% of the maximum THG output, which can be important if polarization-insensitive application is envisioned.

In summary, we have theoretically introduced and experimentally demonstrated a new concept for achieving high-Q dielectric metasurface on a mirror governed by BIC without requiring asymmetric structures. Such a metasurface platform possesses spectrally selective optical absorption with narrow bandwidth, which can be immediately used in applications such as hyper-/multi-spectral photodetection, coupling to quantum emitters, imaging, biosensing,^{21,38} and nonlinear frequency conversion demonstrated in this work. The nonlinear platform is applicable to not only THG shown here but also second order nonlinearities by simply replacing Si by some popular III-V materials with high second-order nonlinear susceptibilities such as GaAs and GaP^{7,26}. Furthermore, other attractive nonlinear processes including ultrafast optical-switching^{27,48}, high harmonic generation (HHG)^{49,50} and the spontaneous parametric down conversion (SPDC)^{51,52} will also benefit from such a simple design. The high degree of geometric symmetry and simplicity makes the platform compatible with low-cost large area fabrication, such as nano-imprinting and interference fringe photolithography.

ASSOCIATED CONTENT

Supporting Information

Supporting Information Available: Detailed methods of simulations, sample fabrication and optical measurements, Eigenfrequency analysis with lossy metal, simulated linear spectra with varied SiO₂ thickness and incident angles, comparison of electric field on two PA points, nonlinear

simulation results with different duration times, ellipsometry measurement results and optical and SEM images of damaged and non-damaged area.

AUTHOR INFORMATION

Corresponding Author

Hayk Harutyunyan - Department of Physics, Emory University, Atlanta, GA 30322, USA

Email: hayk.harutyunyan@emory.edu

Notes

The authors declare no competing financial interest.

ACKNOWLEDGMENT

This work was supported by UDRI with the Air Force contract no. FA8651-20-D-0003. MSA, SUD, and JWA are thankful for the funding support through AFOSR Lab Tasks 22RWCOR002. H.H. acknowledges support from the Department of Energy (DE-SC0020101).

REFERENCES

1. Kuznetsov, A. I.; Miroschnichenko, A. E.; Brongersma, M. L.; Kivshar, Y. S.; Luk'yanchuk, B. Optically resonant dielectric nanostructures. *Science* **2016**, 354, (6314).
2. Shcherbakov, M. R.; Werner, K.; Fan, Z.; Talisa, N.; Chowdhury, E.; Shvets, G. Photon acceleration and tunable broadband harmonics generation in nonlinear time-dependent metasurfaces. *Nature Communications* **2019**, 10, (1), 1-9.
3. Rybin, M. V.; Koshelev, K. L.; Sadrieva, Z. F.; Samusev, K. B.; Bogdanov, A. A.; Limonov, M. F.; Kivshar, Y. S. High-Q supercavity modes in subwavelength dielectric resonators. *Physical Review Letters* **2017**, 119, (24), 243901.
4. Campione, S.; Liu, S.; Basilio, L. I.; Warne, L. K.; Langston, W. L.; Luk, T. S.; Wendt, J. R.; Reno, J. L.; Keeler, G. A.; Brener, I. Broken symmetry dielectric resonators for high quality factor Fano metasurfaces. *ACS Photonics* **2016**, 3, (12), 2362-2367.

5. Yang, Y.; Kravchenko, I. I.; Briggs, D. P.; Valentine, J. All-dielectric metasurface analogue of electromagnetically induced transparency. *Nature Communications* **2014**, *5*, (1), 1-7.
6. Yang, Y.; Wang, W.; Boulesbaa, A.; Kravchenko, I. I.; Briggs, D. P.; Puretzky, A.; Geohegan, D.; Valentine, J. Nonlinear Fano-resonant dielectric metasurfaces. *Nano Letters* **2015**, *15*, (11), 7388-7393.
7. Vabishchevich, P. P.; Liu, S.; Sinclair, M. B.; Keeler, G. A.; Peake, G. M.; Brener, I. Enhanced second-harmonic generation using broken symmetry III–V semiconductor fano metasurfaces. *ACS Photonics* **2018**, *5*, (5), 1685-1690.
8. Hsu, C. W.; Zhen, B.; Stone, A. D.; Joannopoulos, J. D.; Soljačić, M. Bound states in the continuum. *Nature Reviews Materials* **2016**, *1*, (9), 1-13.
9. Koshelev, K.; Lepeshov, S.; Liu, M.; Bogdanov, A.; Kivshar, Y. Asymmetric metasurfaces with high-Q resonances governed by bound states in the continuum. *Physical Review Letters* **2018**, *121*, (19), 193903.
10. Koshelev, K.; Bogdanov, A.; Kivshar, Y. Meta-optics and bound states in the continuum. *Science Bulletin* **2019**, *64*, (12), 836-842.
11. von Neumann, J.; Wigner, E. P., Über merkwürdige diskrete Eigenwerte. In *The Collected Works of Eugene Paul Wigner*, Springer: 1993; pp 291-293.
12. Yin, X.; Jin, J.; Soljačić, M.; Peng, C.; Zhen, B. Observation of topologically enabled unidirectional guided resonances. *Nature* **2020**, *580*, (7804), 467-471.
13. Plotnik, Y.; Peleg, O.; Dreisow, F.; Heinrich, M.; Nolte, S.; Szameit, A.; Segev, M. Experimental observation of optical bound states in the continuum. *Physical Review Letters* **2011**, *107*, (18), 183901.
14. Zhen, B.; Hsu, C. W.; Lu, L.; Stone, A. D.; Soljačić, M. Topological nature of optical bound states in the continuum. *Physical Review Letters* **2014**, *113*, (25), 257401.
15. Hsu, C. W.; Zhen, B.; Chua, S.-L.; Johnson, S. G.; Joannopoulos, J. D.; Soljačić, M. Bloch surface eigenstates within the radiation continuum. *Light: Science & Applications* **2013**, *2*, (7), e84-e84.
16. Liang, Y.; Koshelev, K.; Zhang, F.; Lin, H.; Lin, S.; Wu, J.; Jia, B.; Kivshar, Y. Bound states in the continuum in anisotropic plasmonic metasurfaces. *Nano Letters* **2020**, *20*, (9), 6351-6356.

17. Cong, L.; Singh, R. Symmetry-protected dual bound states in the continuum in metamaterials. *Advanced Optical Materials* **2019**, *7*, (13), 1900383.
18. Sadrieva, Z. F.; Sinev, I. S.; Koshelev, K. L.; Samusev, A.; Iorsh, I. V.; Takayama, O.; Malureanu, R.; Bogdanov, A. A.; Lavrinenko, A. V. Transition from optical bound states in the continuum to leaky resonances: role of substrate and roughness. *ACS Photonics* **2017**, *4*, (4), 723-727.
19. Murai, S.; Abujetas, D. R.; Castellanos, G. W.; Sánchez-Gil, J. A.; Zhang, F.; Rivas, J. G. m. Bound states in the continuum in the visible emerging from out-of-plane magnetic dipoles. *ACS Photonics* **2020**, *7*, (8), 2204-2210.
20. Jahani, Y.; Arvelo, E. R.; Yesilkoy, F.; Koshelev, K.; Cianciaruso, C.; De Palma, M.; Kivshar, Y.; Altug, H. Imaging-based spectrometer-less optofluidic biosensors based on dielectric metasurfaces for detecting extracellular vesicles. *Nature Communications* **2021**, *12*, (1), 1-10.
21. Yesilkoy, F.; Arvelo, E. R.; Jahani, Y.; Liu, M.; Tittl, A.; Cevher, V.; Kivshar, Y.; Altug, H. Ultrasensitive hyperspectral imaging and biodetection enabled by dielectric metasurfaces. *Nature Photonics* **2019**, *13*, (6), 390-396.
22. Hwang, M.-S.; Lee, H.-C.; Kim, K.-H.; Jeong, K.-Y.; Kwon, S.-H.; Koshelev, K.; Kivshar, Y.; Park, H.-G. Ultralow-threshold laser using super-bound states in the continuum. *Nature Communications* **2021**, *12*, (1), 1-9.
23. Kodigala, A.; Lepetit, T.; Gu, Q.; Bahari, B.; Fainman, Y.; Kanté, B. Lasing action from photonic bound states in continuum. *Nature* **2017**, *541*, (7636), 196-199.
24. Koshelev, K.; Tang, Y.; Li, K.; Choi, D.-Y.; Li, G.; Kivshar, Y. Nonlinear metasurfaces governed by bound states in the continuum. *ACS Photonics* **2019**, *6*, (7), 1639-1644.
25. Liu, Z.; Xu, Y.; Lin, Y.; Xiang, J.; Feng, T.; Cao, Q.; Li, J.; Lan, S.; Liu, J. High-Q quasibound states in the continuum for nonlinear metasurfaces. *Physical Review Letters* **2019**, *123*, (25), 253901.
26. Anthur, A. P.; Zhang, H.; Paniagua-Dominguez, R.; Kalashnikov, D. A.; Ha, S. T.; Maß, T. W.; Kuznetsov, A. I.; Krivitsky, L. Continuous wave second harmonic generation enabled by quasi-bound-states in the continuum on gallium phosphide metasurfaces. *Nano Letters* **2020**, *20*, (12), 8745-8751.

27. Karl, N.; Vabishchevich, P. P.; Liu, S.; Sinclair, M. B.; Keeler, G. A.; Peake, G. M.; Brener, I. All-optical tuning of symmetry protected quasi bound states in the continuum. *Applied Physics Letters* **2019**, 115, (14), 141103.
28. Carletti, L.; Kruk, S. S.; Bogdanov, A. A.; De Angelis, C.; Kivshar, Y. High-harmonic generation at the nanoscale boosted by bound states in the continuum. *Physical Review Research* **2019**, 1, (2), 023016.
29. Sinev, I. S.; Koshelev, K.; Liu, Z.; Rudenko, A.; Ladutenko, K.; Shcherbakov, A.; Sadrieva, Z.; Baranov, M.; Itina, T.; Liu, J. Observation of Ultrafast Self-Action Effects in Quasi-BIC Resonant Metasurfaces. *Nano Letters* **2021**, 21, (20), 8848-8855.
30. Bernhardt, N.; Koshelev, K.; White, S. J.; Meng, K. W. C.; Froch, J. E.; Kim, S.; Tran, T. T.; Choi, D.-Y.; Kivshar, Y.; Solntsev, A. S. Quasi-BIC resonant enhancement of second-harmonic generation in WS₂ monolayers. *Nano Letters* **2020**, 20, (7), 5309-5314.
31. Liu, S.; Sinclair, M. B.; Mahony, T. S.; Jun, Y. C.; Campione, S.; Ginn, J.; Bender, D. A.; Wendt, J. R.; Ihlefeld, J. F.; Clem, P. G. Optical magnetic mirrors without metals. *Optica* **2014**, 1, (4), 250-256.
32. Decker, M.; Staude, I.; Falkner, M.; Dominguez, J.; Neshev, D. N.; Brener, I.; Pertsch, T.; Kivshar, Y. S. High-efficiency dielectric Huygens' surfaces. *Adv Opt Mater* **2015**, 3, (6), 813-820.
33. Shcherbakov, M. R.; Neshev, D. N.; Hopkins, B.; Shorokhov, A. S.; Staude, I.; Melik-Gaykazyan, E. V.; Decker, M.; Ezhov, A. A.; Miroshnichenko, A. E.; Brener, I. Enhanced third-harmonic generation in silicon nanoparticles driven by magnetic response. *Nano Letters* **2014**, 14, (11), 6488-6492.
34. Shcherbakov, M. R.; Vabishchevich, P. P.; Shorokhov, A. S.; Chong, K. E.; Choi, D.-Y.; Staude, I.; Miroshnichenko, A. E.; Neshev, D. N.; Fedyanin, A. A.; Kivshar, Y. S. Ultrafast all-optical switching with magnetic resonances in nonlinear dielectric nanostructures. *Nano Letters* **2015**, 15, (10), 6985-6990.
35. Carletti, L.; Koshelev, K.; De Angelis, C.; Kivshar, Y. Giant nonlinear response at the nanoscale driven by bound states in the continuum. *Physical Review Letters* **2018**, 121, (3), 033903.

36. Koshelev, K.; Kruk, S.; Melik-Gaykazyan, E.; Choi, J. H.; Bogdanov, A.; Park, H. G.; Kivshar, Y. Subwavelength dielectric resonators for nonlinear nanophotonics. *Science* **2020**, 367, (6475), 288-292.
37. Melik-Gaykazyan, E.; Koshelev, K.; Choi, J.-H.; Kruk, S. S.; Bogdanov, A.; Park, H.-G.; Kivshar, Y. From Fano to quasi-BIC resonances in individual dielectric nanoantennas. *Nano Letters* **2021**, 21, (4), 1765-1771.
38. Li, W.; Valentine, J. Metamaterial perfect absorber based hot electron photodetection. *Nano Letters* **2014**, 14, (6), 3510-3514.
39. Stewart, J. W.; Vella, J. H.; Li, W.; Fan, S.; Mikkelsen, M. H. Ultrafast pyroelectric photodetection with on-chip spectral filters. *Nature Materials* **2020**, 19, (2), 158-162.
40. Inoue, T.; De Zoysa, M.; Asano, T.; Noda, S. Realization of narrowband thermal emission with optical nanostructures. *Optica* **2015**, 2, (1), 27-35.
41. Lochbaum, A.; Fedoryshyn, Y.; Dorodnyy, A.; Koch, U.; Hafner, C.; Leuthold, J. On-chip narrowband thermal emitter for mid-IR optical gas sensing. *ACS photonics* **2017**, 4, (6), 1371-1380.
42. Haus, H. Waves and fields in optoelectronics. *PRENTICE-HALL, INC., ENGLEWOOD CLIFFS, NJ 07632, USA, 1984, 402* **1984**.
43. Ameling, R.; Langguth, L.; Hentschel, M.; Mesch, M.; Braun, P. V.; Giessen, H. Cavity-enhanced localized plasmon resonance sensing. *Applied Physics Letters* **2010**, 97, (25), 253116.
44. Li, Z.; Butun, S.; Aydin, K. Ultranarrow band absorbers based on surface lattice resonances in nanostructured metal surfaces. *ACS Nano* **2014**, 8, (8), 8242-8248.
45. Yong, Z.; Zhang, S.; Gong, C.; He, S. Narrow band perfect absorber for maximum localized magnetic and electric field enhancement and sensing applications. *Scientific Report* **2016**, 6, (1), 1-7.
46. Anantharaman, S. B.; Stevens, C. E.; Lynch, J.; Song, B.; Hou, J.; Zhang, H.; Jo, K.; Kumar, P.; Blancon, J.-C.; Mohite, A. D.; Hendrickson, J. R.; Jariwala, D. Self-Hybridized Polaritonic Emission from Layered Perovskites. *Nano Letters* **2021**, 21, (14), 6245-6252.

47. Zhang, H.; Abhiraman, B.; Zhang, Q.; Miao, J.; Jo, K.; Roccasecca, S.; Knight, M. W.; Davoyan, A. R.; Jariwala, D. Hybrid exciton-plasmon-polaritons in van der Waals semiconductor gratings. *Nature communications* **2020**, 11, (1), 1-9.
48. Karl, N.; Vabishchevich, P. P.; Shcherbakov, M. R.; Liu, S.; Sinclair, M. B.; Shvets, G.; Brener, I. Frequency conversion in a time-variant dielectric metasurface. *Nano Letters* **2020**, 20, (10), 7052-7058.
49. Liu, H.; Guo, C.; Vampa, G.; Zhang, J. L.; Sarmiento, T.; Xiao, M.; Bucksbaum, P. H.; Vučković, J.; Fan, S.; Reis, D. A. Enhanced high-harmonic generation from an all-dielectric metasurface. *Nature Physics* **2018**, 14, (10), 1006-1010.
50. Zograf, G.; Koshelev, K.; Zalogina, A.; Korolev, V.; Choi, D.-Y.; Zurch, M.; Spielmann, C.; Luther-Davies, B.; Kartashov, D.; Makarov, S. High-harmonic generation from metasurfaces empowered by bound states in the continuum. *arXiv preprint arXiv:2008.11481* **2020** (accessed 2022-01-27).
51. Parry, M.; Mazzanti, A.; Poddubny, A.; Della Valle, G.; Neshev, D. N.; Sukhorukov, A. A. Enhanced generation of non-degenerate photon-pairs in nonlinear metasurfaces. *arXiv preprint arXiv:2104.07299* **2021** (accessed 2022-01-27).
52. Santiago-Cruz, T.; Fedotova, A.; Sultanov, V.; Weissflog, M. A.; Arslan, D.; Younesi, M.; Pertsch, T.; Staude, I.; Setzpfandt, F.; Chekhova, M. Photon Pairs from Resonant Metasurfaces. *Nano Letters* **2021**, 21, (10), 4423-4329.

TOC Graphic

